Supporting Information for:

High-Pressure Single-Crystal Structures of 3D Lead-Halide Hybrid Perovskites and Pressure Effects on their Electronic and Optical Properties

Adam Jaffe,[†] Yu Lin,[†‡§] Christine M. Beavers,[∥] Johannes Voss,[⊥] Wendy L. Mao,[*‡§] and Hemamala I. Karunadasa[*†]

Departments of [†]Chemistry and [‡]Geological Sciences, Stanford University, Stanford, California 94305, United States. [§]Photon Science and Stanford Institute for Materials and Energy Sciences, SLAC National Accelerator Laboratory, Menlo Park, California 94025, United States. [∥]Advanced Light Source, Lawrence Berkeley National Laboratory, Berkeley, California 94720, United States. [⊥]SUNCAT Center for Interface Science and Catalysis, SLAC National Accelerator Laboratory, Menlo Park, California 94025, United States.

*hemamala@stanford.edu, wmao@stanford.edu

Experimental details

Synthesis

Solvents were of reagent grade or higher purity. All reagents were purchased from commercial vendors and used as received. The perovskites $(MA)PbBr_3$, $(MA)PbI_3$, and $(MA)Pb(Br_xI_{1-x})_3$ (x = 0.2, 0.4, or 0.6) were synthesized similarly to reported procedures.[1] All experiments were performed at ambient temperature except when measuring the activation energy of conduction. Abbreviations used: MA = methylammonium.

Diamond-anvil cell (DAC) loading and powder X-ray diffraction (PXRD)

For PXRD measurements at pressures up to ca. 50 GPa, samples were loaded into 100-µm-diameter sample chambers in pre-indented tungsten gaskets, then placed in symmetric DACs with 300-µm culets (i.e., 300-µm face diameter). Ruby spheres were loaded as pressure calibrants and pressure was measured by ruby fluorescence,[2] stimulated by a 100-mW, 447-nm diode laser and measured by a fiber-optic cable coupled to a Princeton Instruments Acton 300i spectrometer. In order to obtain PXRD patterns at finer pressure steps, the same procedure was used with a DAC with 600-µm culets. The larger-culet DAC achieves lower pressures, but can maximize diffractive volume by accommodating more sample. In addition, this DAC has thinner diamonds so that it can access a larger diffraction angle. For both cell types, helium was loaded as a pressure medium using a custom gearbox and gas-loading system. Cells were pressurized to ca. 0.11 GPa with helium and sealed. In situ PXRD was performed at the High-Pressure Beamline (12.2.2) at the Advanced Light Source (ALS) in the Lawrence Berkeley National Laboratory (LBNL). Using a wavelength of 0.4974 Å (25 keV), 2D Debye-Scherrer diffraction rings from powder measurements were collected on a Perkin-Elmer CMOS detector and integrated using the *Dioptas* software package.[3] After each compression or decompression step, the samples were allowed to equilibrate in the DAC until ruby fluorescence (and therefore pressure) was invariant. The pressure was verified again at the end of each diffraction experiment. Peak indexing and space-group determination based on PXRD patterns were performed using the native algorithm in *Jade 2010*[4] and verified using *DICVOL*[5] and *CheckGroup* accessed through *FullProf*[6] and also with *Chekcell*.[7]

Single-crystal structure determination

Ambient-pressure, room-temperature diffraction experiments were conducted on Beamline 11.3.1 at the ALS at LBNL. The single crystals were mounted on MiTeGen® sample mounts, then placed on the goniometer head of a Bruker D85 diffractometer equipped with a Photon 100 CMOS detector. Synchrotron X-rays were monochromated using silicon(111). A full sphere of diffraction data was collected with either 0.6888- or 0.7293-Å X-rays (18 or 17 keV, respectively), using a combination of phi and omega shutterless scans. High-pressure data were collected while the crystal was within a HPDO Merrill-Bassett diamond-anvil cell, equipped with Boehler-Almax cut diamonds, each with an 80° opening angle. Tungsten was used as the gasket material with DuPont Krytox® 1525 as the pressure medium. Ruby spheres were employed for pressure calibration. The loaded DACs were mounted on the Huber sample stages on Beamline 12.2.2. Shutterless, single-crystal diffraction data were collected on a Perkin-Elmer amorphous silicon detector using synchrotron radiation monochromated by silicon(111) to a wavelength of 0.35424 Å (35 keV). Phi scans were employed to measure across both diamonds, with 0.25° image width. Distance and wavelength were calibrated using a NIST single-crystal ruby diffraction

standard.[8] To avoid integrating detector regions obscured by the DAC, image masks were created using the program ECLIPSE.

For both the ambient- and high-pressure data, unit-cell parameters were refined against all data. The crystals did not show significant decay during data collection. Frames were integrated and corrected for Lorentz and polarization effects using SAINT 8.27b, and were corrected for absorption effects using SADABS v2104/5.[9] Space-group assignments were based upon systematic absences, *E*-statistics, agreement factors for equivalent reflections, and successful refinement of the structures. The structures were solved by intrinsic phasing using SHELXT. They were refined against all data using the SHELXL-2014 software package.[10] The high-pressure structure of $(MA)PbBr_3$ required a twin law to refine properly, to account for the loss of centering symmetry. The ambient-pressure, room-temperature $(MA)PbI_3$ structure appears to have tetragonal *I* metric symmetry, but is better behaved in orthorhombic *F* symmetry, with a twin law related to the tetragonal *I* pseudolattice.

Previous reports of $(MA)PbI_3$ detailed refinements in *I4cm* and *I4/mcm*.[1b,11] For both *I4cm* and *I4/mcm*, the reflection conditions in the 0*kl* plane require that both *k* and *l* are even. Our data were initially refined as *I4/mcm*, but the large number of observed data that should have been systematically absent prompted the search for other symmetry (Figure S1). The data were treated as orthorhombic, with all the axes allowed to refine in length independently. All three axes were statistically different in length, with two being more similar. Structure solution in *Fmmm* was successful and the refinement proceeded well when incorporating a twin law relating the orthorhombic *F* cell to the tetragonal *I* cell. The resulting twin fraction was 42(1)%. Since the twin fraction was not 50%, the twin law cannot be considered part of the Laue class and therefore the tetragonal cell is not a correct representation of the crystal symmetry.

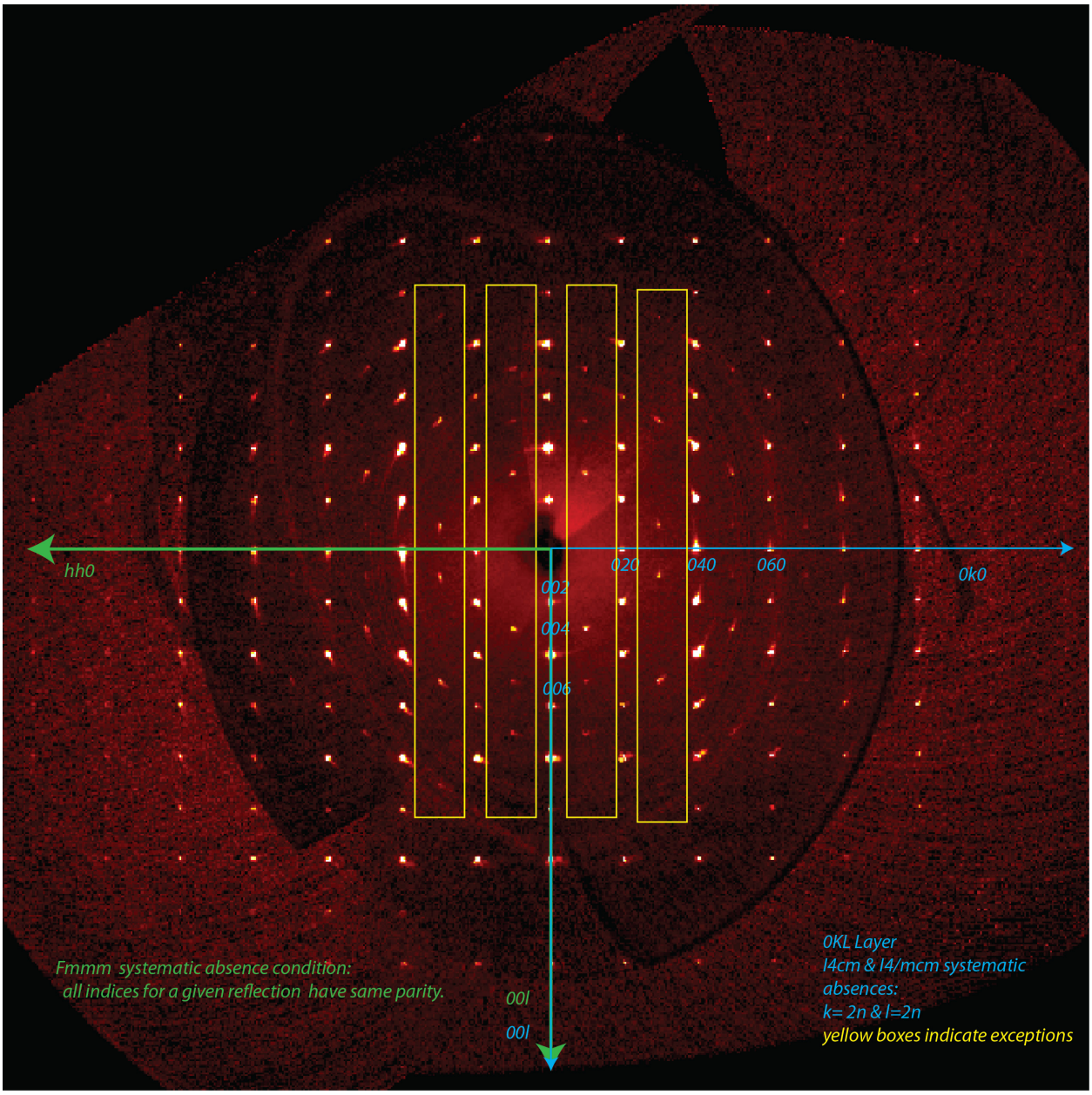

Figure S1. An example of a precession image from the ambient-pressure, room-temperature SCXRD dataset for $(MA)PbI_3$. Systematic absences for *I4cm* and *I4/mcm* are shown in blue and *Fmmm* is shown in green. Relevant exceptions to the systematic absences for *I4cm* and *I4/mcm* are indicated by yellow boxes.

Thermal parameters for all lead and halide atoms were refined anisotropically, unless disorder made this unreasonable. In the case of both the ambient- and high-pressure $(MA)PbI_3$ structures, the shape of the electron density surrounding the iodine sites indicated the presence of disorder. In the case of the ambient-pressure data set, two of the three iodine sites had oddly shaped electron density (see Figure S2). Splitting these sites in a disorder model significantly improved the refinement. In the high-pressure structure, the structure gains symmetry, and transforms to cubic *I* symmetry, which condenses all three iodine positions down into one. This one site displays high disorder, which appears similar to a superposition of the three sites in the room-pressure data set (Figure S3).

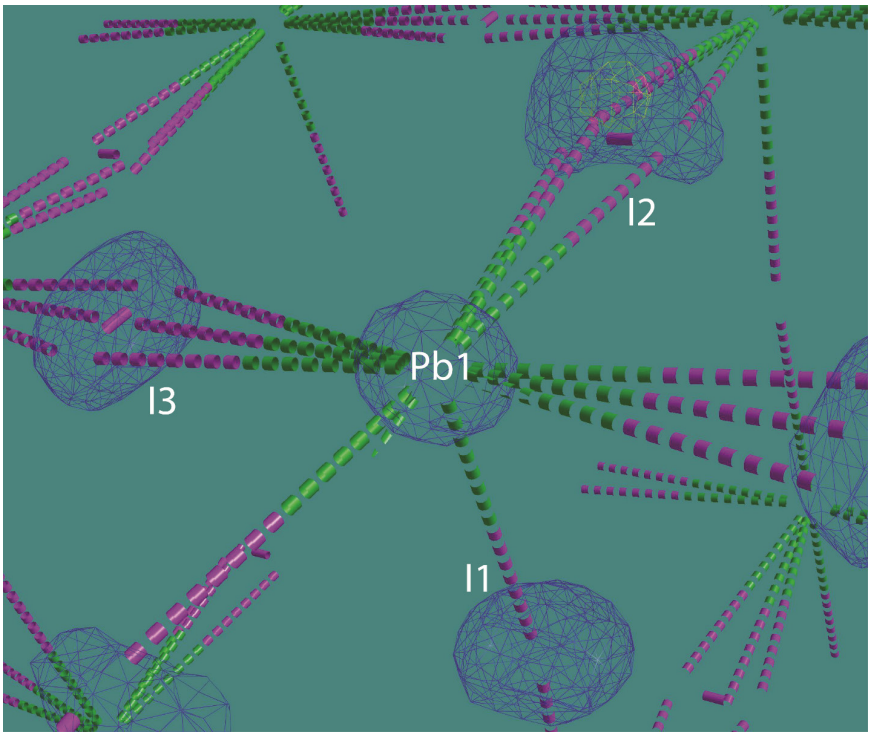

Figure S2. F_{obs} map of the ambient-pressure structure of (MA)PbI_3, demonstrating the atypical electron-density shapes.

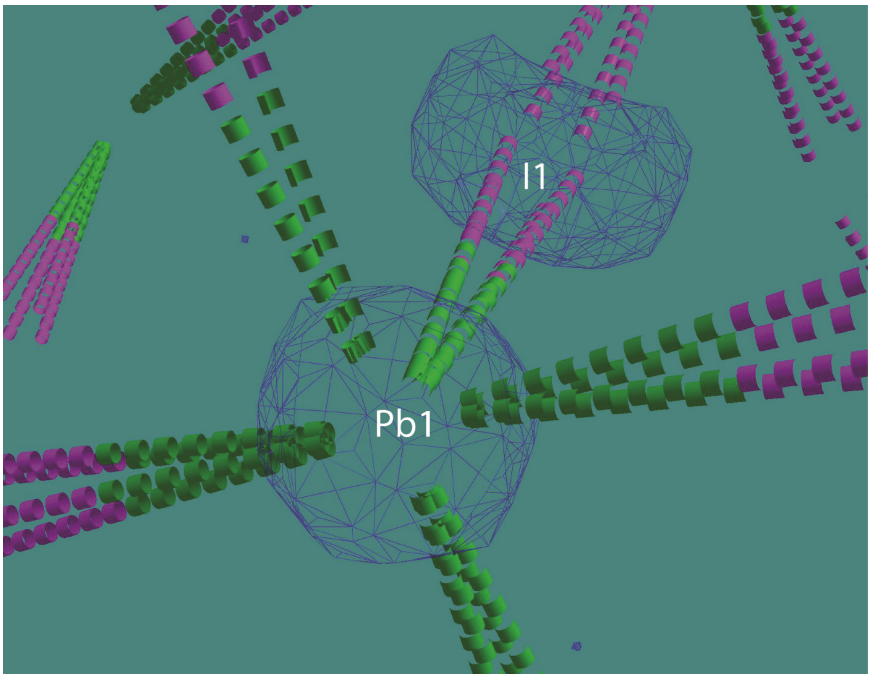

Figure S3. F_{obs} map of the 0.7-GPa structure of (MA)PbI_3, illustrating the non-ellipsoid shape of the electron density.

Determining the methylammonium positions in the difference map was done using $F_{obs} - F_{calc}$ maps in both SHELXLE and winCoot. In many cases, the nitrogen and the carbon positions were on symmetry related sites. Restraints were used to keep the two light atoms from migrating to the center of their bonding density. Hydrogens were not found in the difference map, so they were not refined.

Subsequent Rietveld refinements were either performed in *FullProf*[6] or *Jade 2010*[4] by inputting SCXRD crystallographic information files (CIFs) of the α or β phases of (MA)$PbBr_3$ or (MA)PbI_3 as initial models, which were then refined to fit experimental PXRD patterns. Spline backgrounds were determined manually and the following parameters were each individually allowed to refine, followed by simultaneous refinement of all parameters: scale factor, lattice parameters, peak-shape parameters according to a Thompson-Cox-Hastings pseudo-Voigt or a Pearson model function, preferred orientation, Pb and halide atomic positions (if not occurring on a special position), and Pb and halide thermal parameters. CIFs were then generated for further structural analysis.

Photoluminescence (PL) spectroscopy

High-pressure PL spectroscopy was performed on a Renishaw RM1000 Raman microscope using a 514.5-nm laser excitation line at 1.75 μW with a ~5-μm spot size, using samples loaded into the DACs with 600-μm culets. Helium was used as a pressure-transmitting medium as described above. Light-exposure PL experiments were performed over a range from 1.5 to 2.2 eV with spectral acquisitions approximately every eight seconds. PL measurements for (MA)PbI_3 employed longer scans of approximately one minute over a range from 1.38 to 1.9 eV.

High-pressure resistivity measurements

Solid (MA)PbI_3 was loaded into an insulating boron nitride gasket onto which four platinum leads were overlaid. These leads extended into the sample cavity in a van der Pauw conformation. This gasket was then mounted into a cross-type DAC and the platinum leads were connected with solder to external leads, which were connected in turn to a Bio-Logic VSP 300 potentiostat/galvanostat. To cool to lower temperatures, the DAC was placed on a steel block, the bottom of which was immersed in a Thermo NESLAB CB-80 cryo-bath. The sample temperature was determined using a type-K thermocouple fixed to the back face of the diamond in the DAC. An elevated temperature measurement was obtained by placing the DAC in an oven with the leads and the thermocouple exiting through an external port. Measurements were acquired once the temperature of the diamond was invariant. Temperature limits of 246 to 315 K were used in order to avoid excessive thermal expansion/contraction of the gasket and/or diamonds, which could also alter sample geometry. Two-point measurements were acquired by obtaining current-voltage curves over a range of –40 to 40 mV at a scan rate of 1 $mV \cdot s^{-1}$ at each temperature and the conductivity was then calculated using the slope of the averaged curves as well as sample thickness and distance between leads. Final two-point conductivities were then calculated by averaging values obtained between multiple sets of two different leads. Four-point conductivity measurements were also acquired to confirm whether contact resistance was negligible. A constant current of 100 μA was passed between two adjacent leads while voltage was measured across the other two according to the van der Pauw method. Two resistance values are required to calculate sheet resistance R_s: a horizontal resistance R_h found by measuring voltage across the first and second leads, then a vertical resistance R_v from the voltage across the second and third leads, for example. Here, R_s (Ω) is given by the following equation:

$$e^{-\pi R_h/R_s} + e^{-\pi R_v/R_s} = 1$$

From R_s, one can then calculate resistivity, ρ (Ω·cm), by multiplying R_s by the thickness, t (cm).

Bulk modulus determination using the Birch-Murnaghan Equation of State (BM EOS)

High-pressure PXRD experiments show how the unit-cell parameters and cell volume vary with pressure. The pressure-volume relationship is known as the isothermal equation of state (EOS), which is usually parameterized in terms of the bulk modulus and its pressure derivative evaluated at ambient pressure. For most solids that undergo moderate compression ($V/V_0 > 0.6$), the Birch-Murnaghan (BM) EOS provides a generally accurate representation of the volume variation with pressure.[12] The BM EOS is one type of finite strain EOS based on the assumption that the strain energy of a solid undergoing compression can be expressed as a Taylor series expansion, accounting for non-linear behavior, in the Eulerian strain (strain according to a spatial reference rather than material-dependent reference). Expansion to second order in the Eulerian strain yields a second-order BM EOS:

$$P(V) = \frac{3}{2} K_0 \left[\left(\frac{V_0}{V} \right)^{\frac{7}{3}} - \left(\frac{V_0}{V} \right)^{\frac{5}{3}} \right]$$

where P is pressure, V is volume, V_0 is initial volume, and K_0 is the bulk modulus at ambient pressure. The second-order BM EOSs fit our data with high goodness of fit. Because further expansion of the EOS to higher order does not yield better fitting statistics and can lead to over-parameterization or unstable fits, we consider the second-order BM EOS to be adequate for representing the data.

Electronic structure calculations

Electronic structures were calculated using the plane-wave DFT code Quantum Espresso.[13] Bandgaps were predicted using the GLLBsc[14] modification of the GLLB functional[15] allowing for a particle number derivative discontinuity correction of DFT fundamental gaps. Kohn-Sham[16] wave functions were expanded in basis sets with a plane-wave cut-off of 600 eV and ionic cores were described by ultrasoft pseudopotentials.[17] Brillouin zone sampling was performed with mesh spacings of at most ~0.01 $Å^{-1}$. Besides relativistic contributions to the pseudopotentials, spin-orbit interactions were only considered for bands with Pb 6*p* or I 5*p* character (see below for details about the corresponding atomic projection scheme used).

Crystal structures used in the DFT calculations

For the α phase of (MA)PbI_3, we used SCXRD and Rietveld refinements in *Fmmm* symmetry as input. We only allowed the I atoms with free Wyckoff coordinates (i.e., not in special positions) to relax, preventing the Pb–I network from responding to the symmetry-lowering due to the non-disordered proton positions of MA. We also performed DFT calculations, where we substituted Cs^+ for MA. Here, we symmetrized the I positions obtained from the structural relaxation mentioned above, i.e., we restored the symmetry that was broken by proton placement by making the I positions with free Wyckoff coordinates equivalent. With this treatment, switching from Cs^+ to MA does not lead to qualitative changes in the band structure (Figure S13). We therefore also chose to use Cs^+ as the cation in the β phase, mimicking the rotational disorder of MA in this phase. As we do not consider MA in the β phase for the calculations,

we relied on the experimental fit as input for the I positions in the lattice, since relaxation with the smaller Cs^+ overestimates Pb–I octahedral rotations. To reduce scatter in these atomic coordinates, we performed second-order fits of the unit-cell volume and the two free iodide Wyckoff coordinates as a function of pressure (Figure S12).

Treatment of spin-orbit coupling

We considered spin-orbit interactions in the *LS* coupling limit, i.e., we assumed spin-orbit interactions can be considered as a perturbation to the electronic system interacting via Coulomb forces. The spin-orbit Hamiltonian for the *LS* coupling case for an atom is given below in atomic Hartree units (See for example, Messiah)[18]:

$$\hat{V}_{\mathrm{SO}} = \frac{\alpha^2}{2r}\frac{dV}{dr}\,|r\rangle\langle r|\hat{\boldsymbol{L}}\cdot\hat{\boldsymbol{S}}$$

Here, V is the potential around the nucleus at distance r, α is the fine-structure constant, and $\hat{\boldsymbol{L}}$ and $\hat{\boldsymbol{S}}$ are operators for electron angular momentum and spin, respectively. Several DFT codes evaluate $(1/r)\cdot(dV/dr)$ on radial grids around the nuclei in the unit cell. We chose instead to consider the r-dependent pre-factor of the spin-orbit Hamiltonian as a parameter A_p we separately define for each nuclear species and angular-momentum channel:

$$\hat{V}_{\mathrm{SO}} = \sum_{m,m'} A_p\,\langle m|\hat{\boldsymbol{L}}\cdot\hat{\boldsymbol{S}}\,|m'\rangle\,|m\rangle\langle m'|$$

We considered different values for A_p for the $6p$ states of Pb and the $5p$ states of I, respectively. Here, $|m\rangle$ and $|m'\rangle$ are atomic $6p$ and $5p$ wavefunctions centered at each Pb and I atom in the unit cell, respectively (spin indices suppressed for clarity). The total spin-orbit interaction on the valence electrons in the solid is thus given as the sum over individual $\hat{V}_{\mathrm{SO}}$, each centered on all Pb and I atoms in the unit cell.

We determined the values for A_p by performing PBEsol[19] calculations including the above $\hat{V}_{\mathrm{SO}}$ and comparing to halide bandgaps obtained using fully relativistic PBEsol pseudopotentials.[20] To distinguish the effect of spin-orbit interactions for Pb and I, we first calculated the bandgap of $CsPbBr_3$ at several pressures, neglecting spin-orbit effects for the $4p$ states of Br. A value of $A_p^{\mathrm{Pb}} \approx 0.06\ a.u.$ reproduces the fully relativistic PBEsol results well. We use a much smaller value of $A_p^{\mathrm{I}} \approx 0.01\ a.u.$ for I.

GW calculations using fully relativistic pseudopotentials have been shown to yield bandgaps in good agreement with experiments for $(MA)PbI_3$ and $(MA)SnI_3$.[21] We chose here to use the computationally more efficient GLLBsc approach[14] and supplement it with $\hat{V}_{\mathrm{SO}}$ defined above. This allowed us to use scalar-relativistic GLLBsc pseudopotentials. In fact, assuming the absence of magnetic moments, we can take advantage of the imposed time-reversal symmetry and the resulting doubly degenerate bands to trace out spin from the band-structure calculations completely. This density-functional approach also allows us to increase the Brillouin-zone sampling density non-self-consistently at little computational cost, such that accurate density of states and electronic dispersion calculations can be performed very efficiently. We can thus use this approach to efficiently calculate bandgaps of the lead halides as a function of pressure, as we have shown in this article.

Table S1. Crystallographic data[a] for $(MA)PbBr_3$ and $(MA)PbI_3$

	α-$(MA)PbBr_3$, ambient *P*	**β-$(MA)PbBr_3$, 1.7 GPa**	**α-$(MA)PbI_3$, ambient *P***	**β-$(MA)PbI_3$, 0.7 GPa**
Empirical Formula	CH_6NPbBr_3	CH_6NPbBr_3	CH_6NPbI_3	CH_6NPbI_3
Wavelength, Å	0.7293	0.3542	0.6888	0.3542
Formula Weight, $g \cdot mol^{-1}$	478.99	478.99	619.96	619.96
Temperature, K	296	296	296	296
Crystal System	Cubic	Cubic	Orthorhombic	Cubic
Space group	$Pm\bar{3}m$	$Im\bar{3}$	$Fmmm$	$Im\bar{3}$
a, Å	5.9328(14)	11.500(5)	12.4984(7)	12.3053(9)
b, Å	5.9328(14)	11.500(5)	12.5181(7)	12.3053(9)
c, Å	5.9328(14)	11.500(5)	12.6012(8)	12.3053(9)
$\alpha = \beta = \gamma$, °	90	90	90	90
Volume, $Å^3$	208.82(15)	1521(2)	1971.5(2)	1863.3(4)
Z	1	8	8	8
Density (calculated), $g \cdot cm^{-3}$	3.809	4.183	4.177	4.420
Absorption coefficient, mm^{-1}	34.34	37.71	26.19	11.46
$F(000)$	206	1648	2080	2080
Crystal size, mm^3	0.03 × 0.02 × 0.01	0.06 × 0.06 × 0.05	0.05 × 0.05 × 0.05	0.02 × 0.02 × 0.01
θ range, °	3.5 to 34.1	2.2 to 14.6	2.7 to 35.0	1.7 to 13.6
Index ranges	$-9 \le h \le 9$ $-9 \le k \le 9$ $-9 \le l \le 9$	$-15 \le h \le 15$ $-16 \le k \le 16$ $-15 \le l \le 15$	$-20 \le h \le 20$ $-20 \le k \le 20$ $-20 \le l \le 20$	$-7 \le h \le 7$ $-16 \le k \le 16$ $-16 \le l \le 16$
Reflections collected/unique	4451/113	7461/415	7622/1326	5640/418
Completeness to θ_{max}, %	100	94.3	99.8	94.9
Data/parameters/restraints	113/10/3	415/14/1	1326/24/1	418/51/38
Goodness-of-fit on F^2	1.27	1.20	1.11	1.15
Final R indices [$I > 2\sigma(I)$][b]	$R_1 = 0.0153$ $wR_2 = 0.0408$	$R_1 = 0.0607$ $wR_2 = 0.1562$	$R_1 = 0.0555$ $wR_2 = 0.1831$	$R_1 = 0.0949$ $wR_2 = 0.2824$
R indices (all data)[b]	$R_1 = 0.0153$ $wR_2 = 0.0408$	$R_1 = 0.0891$ $wR_2 = 0.1765$	$R_1 = 0.0731$ $wR_2 = 0.1948$	$R_1 = 0.1138$ $wR_2 = 0.3255$
Largest diff. peak and hole, $e \cdot Å^{-3}$	0.46, −0.59	2.24, −2.10	3.26, −5.66	4.68, −3.22

[a] Obtained at ALS Beamlines 12.2.2 or 11.3.1

[b] $R_1 = \Sigma||F_o| - |F_c||/\Sigma|F_o|$, $wR_2 = [\Sigma w(F_o^2 - F_c^2)^2/\Sigma(F_o^2)^2]^{1/2}$

Table S2. Structural information for $(MA)PbBr_3$ derived from SCXRD structures and Rietveld refinements. Relevant information for Rietveld refinements is provided. Information for the SCXRD structures at 0 and 1.7 GPa is shown above in Table S1.

	~0 GPa (SC)	**0.4 GPa**	**0.7 GPa**	**1.0 GPa**	**1.3 GPa**	**1.7 GPa (SC)**	**2.3 GPa**
Number of reflections	-	44	42	147	151	-	144
Space Group	$Pm\bar{3}m$	$Pm\bar{3}m$	$Pm\bar{3}m$	$Im\bar{3}$	$Im\bar{3}$	$Im\bar{3}$	$Im\bar{3}$
Weighted *R*-value (%)	-	5.65	4.66	4.98	3.91	-	4.34
a, Å	5.9328(14)	5.8808(2)	5.8550(2)	11.6142(5)	11.5324(5)	11.500(5)	11.3358(6)
b, Å	5.9328(14)	5.8808(2)	5.8550(2)	11.6142(5)	11.5324(5)	11.500(5)	11.3358(6)
c, Å	5.9328(14)	5.8808(2)	5.8550(2)	11.6142(5)	11.5324(5)	11.500(5)	11.3358(6)
$a = \beta = \gamma$, °	90	90	90	90	90	90	90
V, Å^3	208.82(15)	203.38(2)	200.72(2)	1566.6(2)	1533.8(2)	1521(2)	1456.7(3)
Pb–Br–Pb angle (θ_R, °)	180	180	180	161.799(2)	157.274(1)	159.769(7)	154.903(3)
Pb–Br distance (Å)	2.9664(7)	2.9403(0)	2.9275(0)	2.9406(1)	2.9407(1)	2.920(2)	2.9033(8)

Table S3. Structural information for $(MA)PbI_3$ derived from SCXRD structures and Rietveld refinements. Relevant information for Rietveld refinements is provided. Information for the SCXRD structures at 0 and 0.7 GPa is shown above in Table S1.

	~0 GPa (SC)	**0.1 GPa**	**0.6 GPa**	**0.7 GPa (SC)**	**1.1 GPa**	**1.8 GPa**	**2.3 GPa**
Number of reflections	-	226	150	-	160	155	161
Space Group	*Fmmm*	*Fmmm*	$Im\bar{3}$	$Im\bar{3}$	$Im\bar{3}$	$Im\bar{3}$	$Im\bar{3}$
Weighted *R*-value	-	5.86	5.20	-	1.72	2.31	1.73
a, Å	12.4984(7)	12.477(4)	12.365(1)	12.3053(9)	12.2285(4)	12.0920(4)	12.0053(3)
b, Å	12.5181(7)	12.472(2)	12.365(1)	12.3053(9)	12.2285(4)	12.0920(4)	12.0053(3)
c, Å	12.6012(8)	12.631(2)	12.365(1)	12.3053(9)	12.2285(4)	12.0920(4)	12.0053(3)
$a = \beta = \gamma$, °	90	90	90	90	90	90	90
V, Å^3	1971.5(2)	1965.5(7)	1890.4(6)	1863.3(4)	1828.6(2)	1768.1(2)	1730.28(1)
Pb–I–Pb angle along *c* axis (θ_c, °, majority position)	180	180	-	-	-	-	-
Average Pb–I–Pb angle in *ab* plane (θ_{ab}, °)	163.534(1)	163.528(4)	-	-	-	-	-
Average Pb–I–Pb angle (θ_R, °)	-	-	154.9(4)	154.9(8)	153.56(4)	151.52(7)	150.78(4)
Average Pb–I distance (Å)	3.163(2)	3.159(1)	3.18(1)	3.16(3)	3.153(2)	3.13(1)	3.116(2)

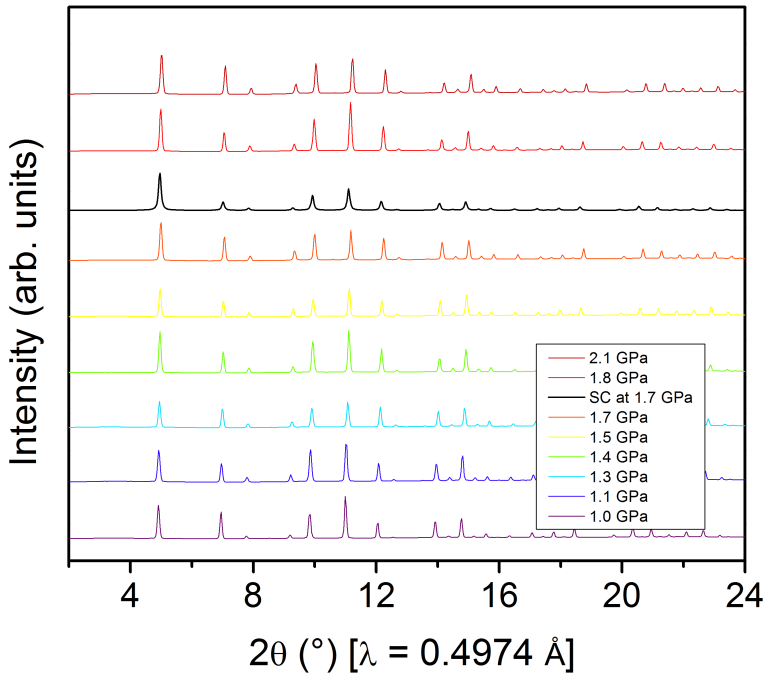

Figure S4. Comparison of experimental PXRD patterns of $(MA)PbBr_3$ upon compression between 1.0 and 2.1 GPa with the predicted powder pattern at 1.7 GPa based on the SCXRD structure solution.

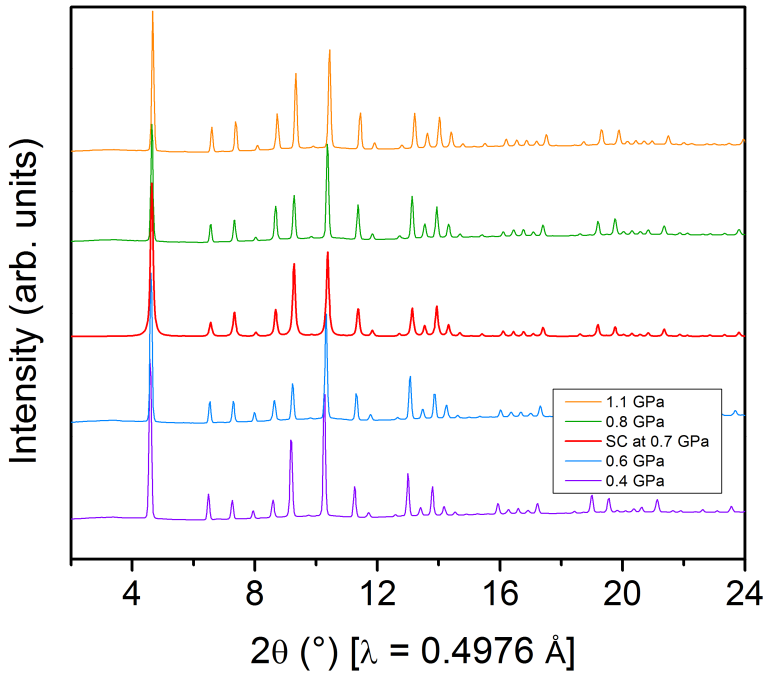

Figure S5. Comparison of experimental PXRD patterns of $(MA)PbI_3$ upon compression between 0.4 and 1.1 GPa with the predicted powder pattern at 0.7 GPa based on the SCXRD structure solution.

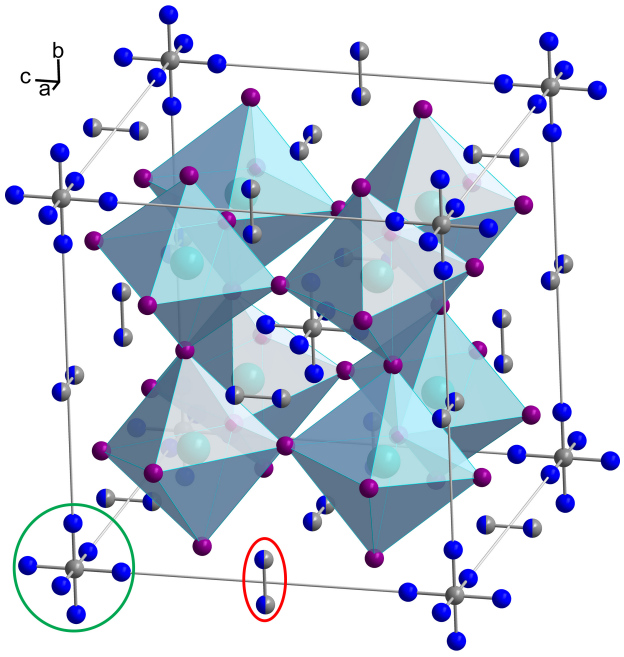

Figure S6. SCXRD structure of β-(MA)PbI_3 at 0.7 GPa with inequivalent MA sites indicated by red and green ellipses. Turquoise, purple, gray, and blue spheres represent Pb, I, C and N atoms, respectively. The C and N positions are disordered. Iodide disorder is not shown for clarity. The green MA site displays more spherically symmetric, rotational disorder whereas the red site only displays 50:50 disorder between C and N as indicated by the half-blue, half-gray spheres.

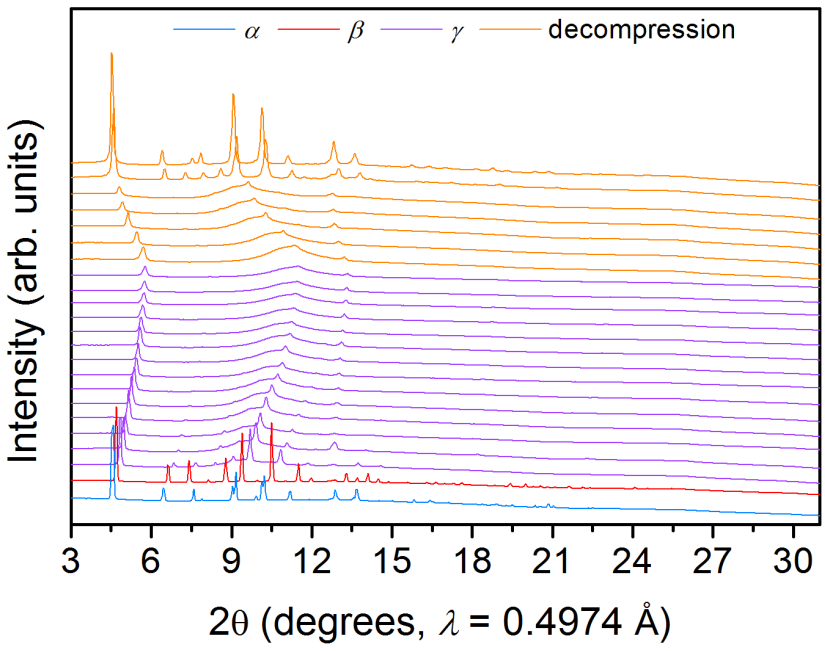

Figure S7. PXRD patterns of (MA)PbI_3 upon compression up to 48.5 GPa. The pressures for each phase (in GPa) are α (0.4), β (1.5), and γ (3.2 to 48.5).

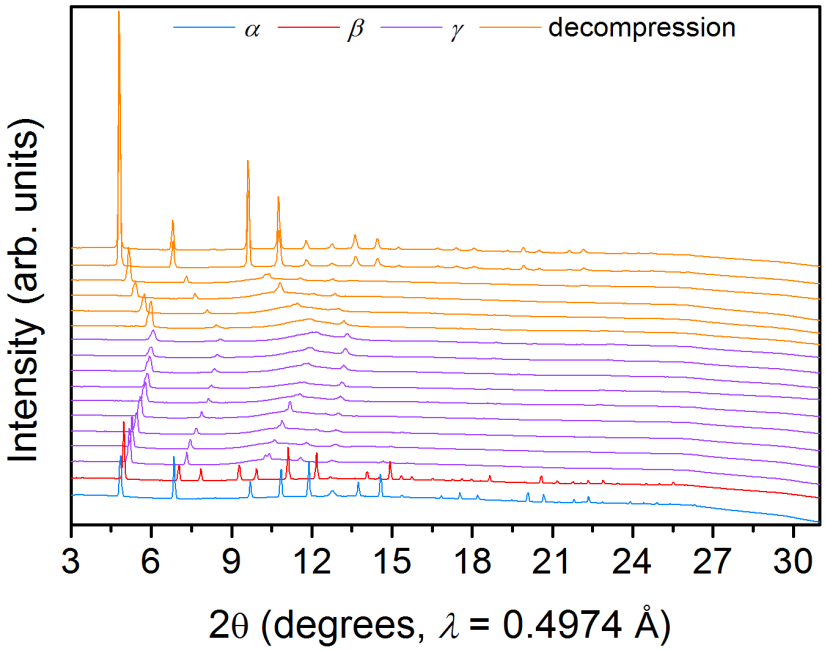

Figure S8. PXRD patterns of (MA)$PbBr_3$ upon compression up to 46.4 GPa. The pressures for each phase (in GPa) are α (0.6), β (1.5), and γ (3.9 to 46.4).

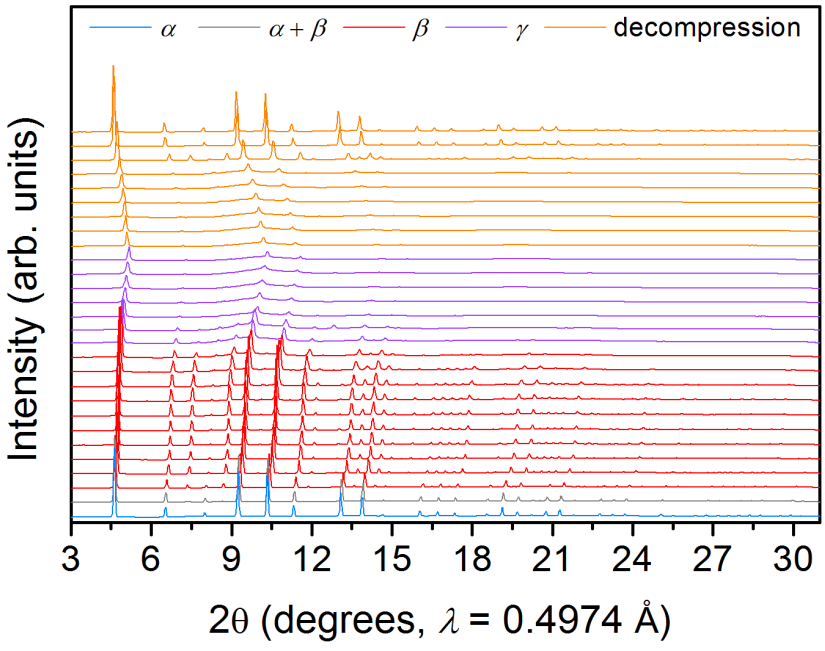

Figure S9. PXRD patterns of (MA)$Pb(Br_{0.2}I_{0.8})_3$ upon compression up to 9.0 GPa. The pressures for each phase (in GPa) are α (0.3), α+β (0.4), β (0.5 to 2.8), and γ (3.1 to 9.0).

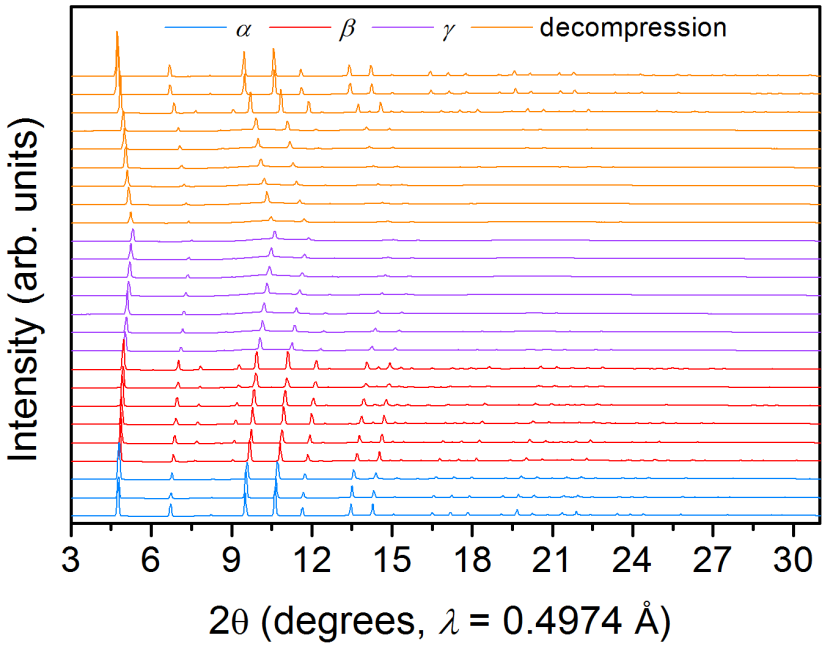

Figure S10. PXRD patterns of (MA)Pb($Br_{0.6}I_{0.4}$)$_3$ upon compression up to 9.0 GPa. The pressures for each phase (in GPa) are α (0.2 to 0.6), β (0.9 to 2.5), and γ (2.7 to 9.0).

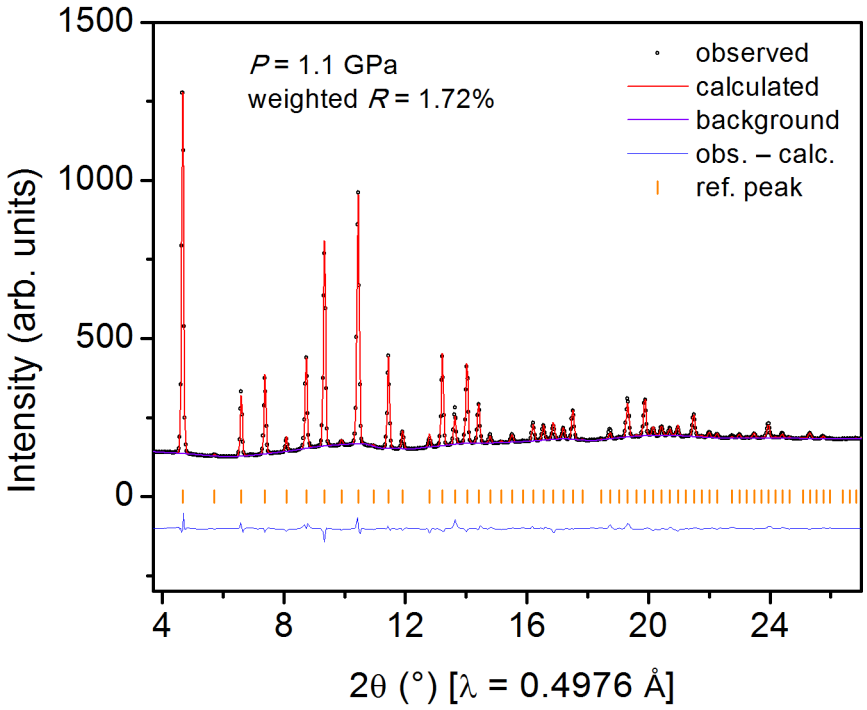

Figure S11. Example of a Rietveld refinement fit for the β phase of (MA)PbI_3 at 1.1 GPa. Refinements performed for both (MA)$PbBr_3$ and (MA)PbI_3 yielded similar fits.

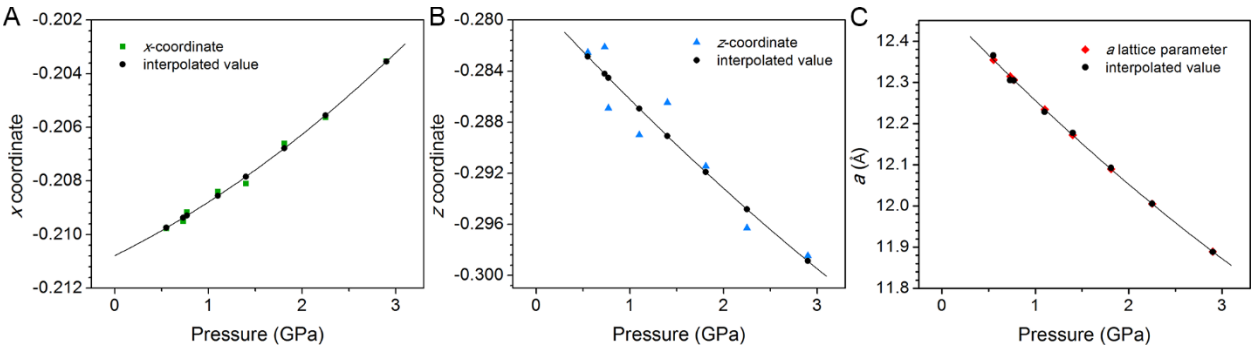

Figure S12. Rietveld refinement-derived values (colored) and interpolated values (black) for the *x* and *z* Wyckoff coordinates of the iodide atom and the *a* lattice parameter in the *β* phase of (MA)PbI_3. The six-fold disorder of the iodide position observed in the SCXRD structure was too complex to simulate in DFT calculations. Therefore, we performed separate Rietveld refinements (not used for the structural discussion) using a single iodide position. These refinements are only approximations of the true structure and the interpolated values provide a more likely, smooth trend as a function of pressure, which was used for the DFT calculations.

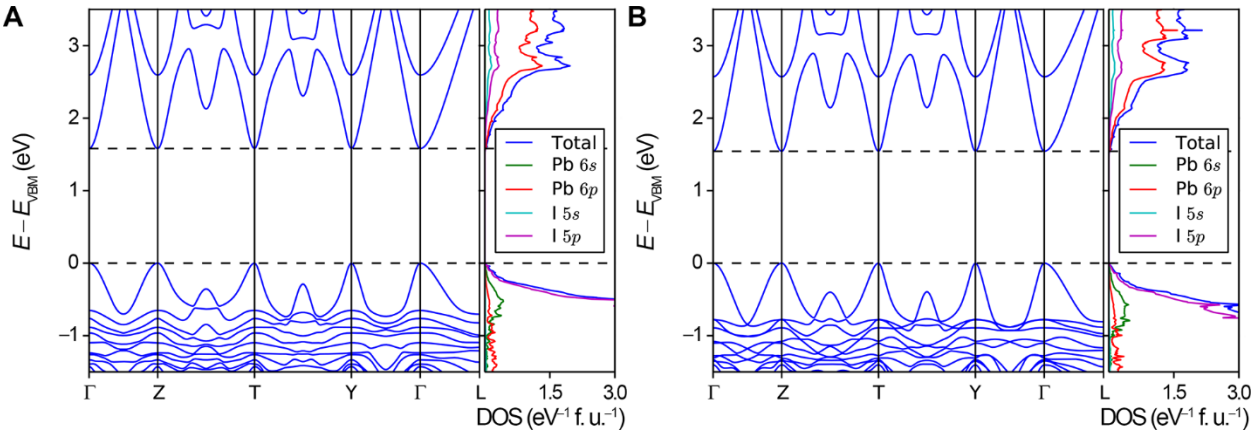

Figure S13. A) Electronic structure and density of states for the DFT-relaxed structure of (MA)PbI_3 at 0 GPa. B) Electronic structure and density of states for the same structure but with Cs^+ placed in the MA site. The Cs^+ position was allowed to relax but the rest of the structure was not allowed to relax further. Note that the electronic structures appear very similar.

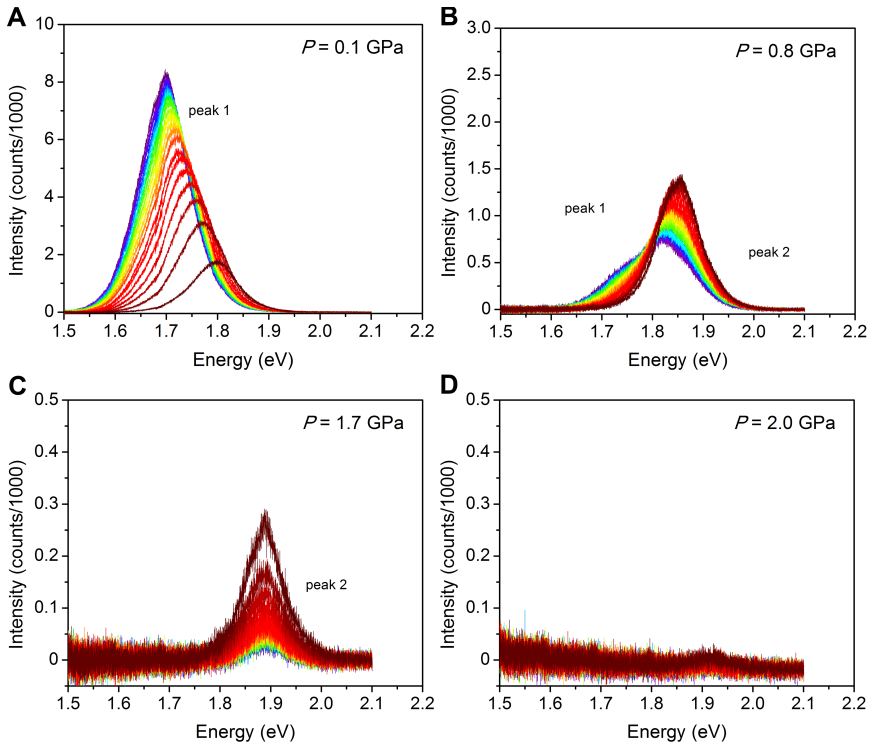

Figure S14. PL spectra recorded at ca. 8-s intervals for (MA)Pb($Br_{0.4}I_{0.6}$)$_3$ showing the evolution of the PL as a function of light soaking. Spectra displayed were obtained at A) 0.1 GPa, B) 0.8 GPa, C) 1.7 GPa, and D) 2.0 GPa.

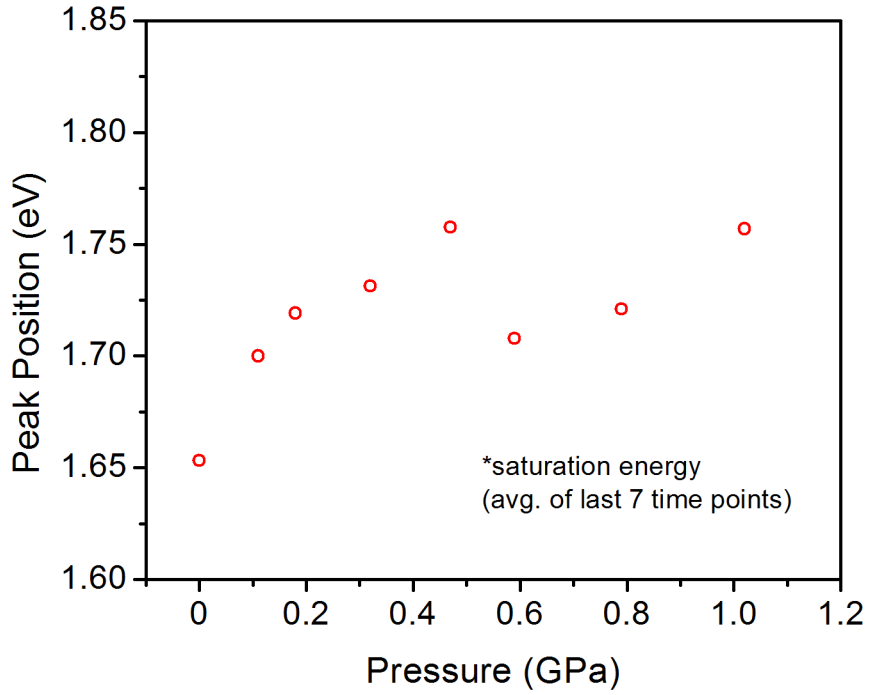

Figure S15. Pressure dependence of peak 1's saturation energy (energy to which the PL band asymptotes with light exposure) for (MA)Pb($Br_{0.4}I_{0.6}$)$_3$.

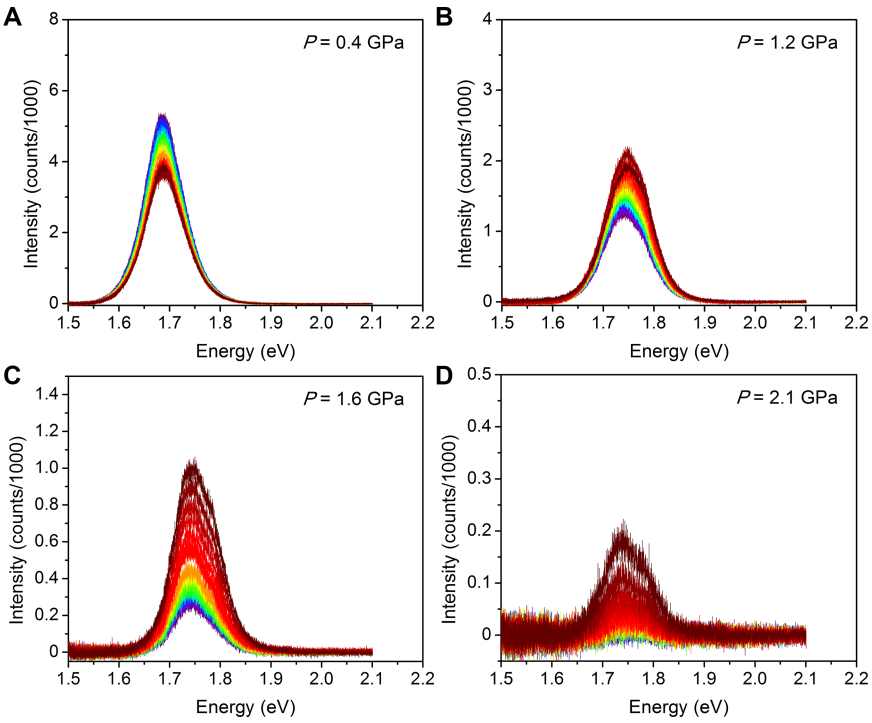

Figure S16. PL spectra recorded at ca. 8-s intervals for (MA)Pb($Br_{0.2}I_{0.8}$)$_3$ showing the evolution of the PL as a function of light soaking. Spectra displayed were obtained at A) 0.4 GPa, B) 1.2 GPa, C) 1.6 GPa, and D) 2.1 GPa.

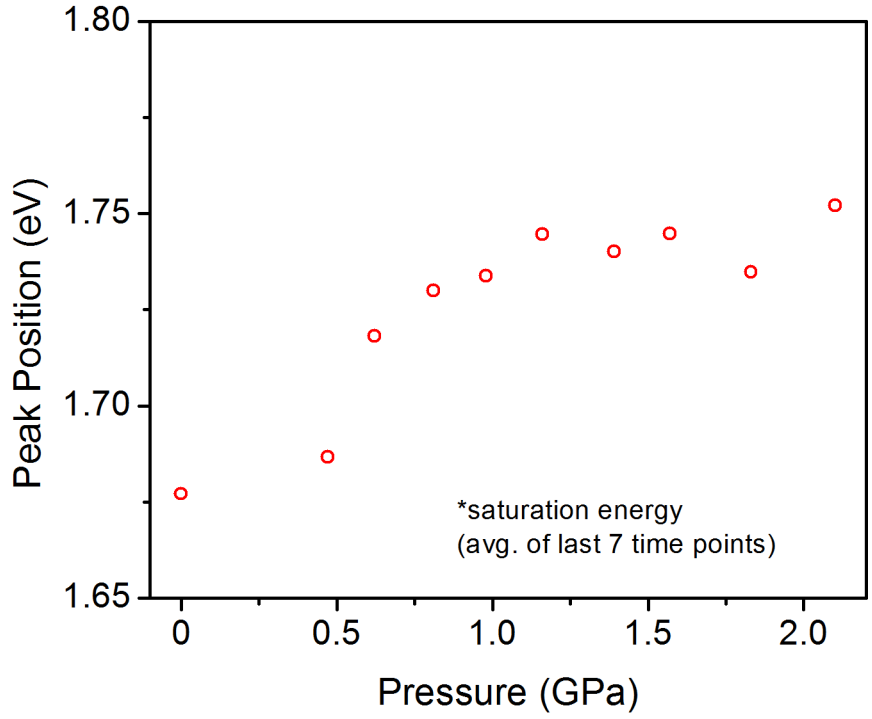

Figure S17. Pressure dependence of peak 1's saturation energy (energy to which the PL band asymptotes with light exposure) for (MA)Pb($Br_{0.2}I_{0.8}$)$_3$.

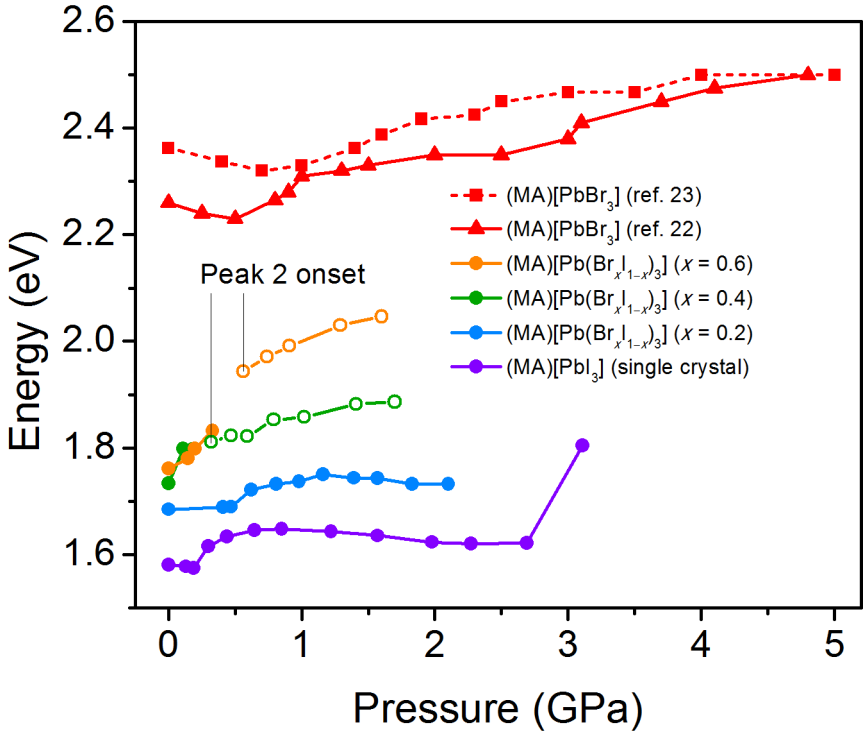

Figure S18. Evolution of initial PL peak energy for (MA)Pb(Br_xI_{1-x})$_3$ (x = 0, 0.2, 0.4, 0.6, 1) as a function of pressure. For the x = 0.4 and x = 0.6 materials, peak 1 is shown with filled symbols and the onset for peak 2 (open symbols) is marked.

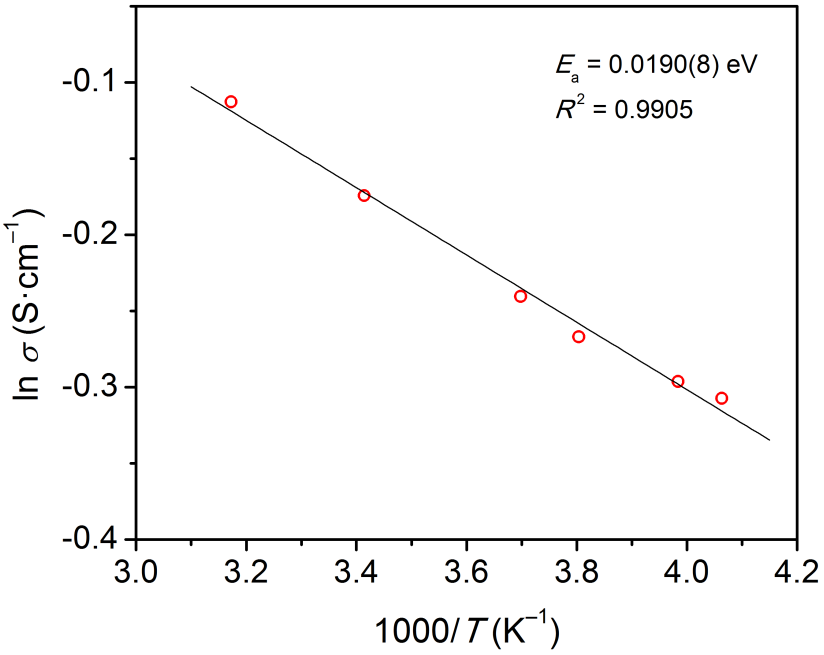

Figure S19. Arrhenius fit of the natural logarithm of conductivity vs. inverse temperature at 47 GPa. The linear fit gives an activation energy of conduction of 19.0(8) meV.

References

(1) (a) Hoke, E. T.; Slotcavage, D. J.; Dohner, E. R.; Bowring, A. R.; Karunadasa, H. I.; McGehee, M. D. Reversible photo-induced trap formation in mixed-halide hybrid perovskites for photovoltaics. *Chem. Sci.* **2015**, *6*, 613-617. (b) Noh, J. H.; Im, S. H.; Heo, J. H.; Mandal, T. N.; Seok, S. I. Chemical management for colorful, efficient, and stable inorganic–organic hybrid nanostructured solar cells. *Nano Lett.* **2013**, *13*, 1764-1769.

(2) Mao, H. K.; Xu, J.; Bell, P. M. Calibration of the ruby pressure gauge to 800 kbar under quasi-hydrostatic conditions. *J. Geophys. Res. B* **1986**, *91*, 4673-4676.

(3) Prescher, C.; Prakapenka, V. B. DIOPTAS: a program for reduction of two-dimensional X-ray diffraction data and data exploration. *High Pressure Res.* **2015**, *35*, 223-230.

(4) *Jade 2010*; Materials Data Inc.: Livermore, CA, USA, **2015**.

(5) Boultif, A.; Louer, D. Powder pattern indexing with the dichotomy method. *J. Appl. Crystallogr.* **2004**, *37*, 724-731.

(6) Rodríguez-Carvajal, J. Recent advances in magnetic structure determination by neutron powder diffraction. *Physica B* **1993**, *192*, 55-69.

(7) Laugier, J.; Bochu, B. *Chekcell*; Laboratoire des Matériaux et du Génie Physique Ecole Nationale Supérieure de Physique de Grenoble (INPG): Saint Martin d'Hères, France, **2004**.

(8) Wong-Ng, W.; Siegrist, T.; DeTitta, G. T.; Finger, L. W.; Evans Jr., H. T.; Gabe, E. J.; Enright, G. D.; Armstrong, J. T.; Levenson, M.; Cook, L. P.; Hubbard, C. R. Standard reference material (SRM 1990) for single crystal diffractometer alignment. *J. Res. Natl. Inst. Stand. Technol.* **2001**, *106*, 1071-1095.

(9) *SAINT and SADABS*; Bruker AXS Inc.: Madison, Wisconsin, **2007**.

(10) (a) Sheldrick, G. M. A short history of SHELX. *Acta. Cryst. Sect. A* **2008**, *64*, 112-122. (b) Muller, P., Herbst-Irmer, R., Spek, A. L., Schneider, T. R., Sawaya, M. R. *Crystal Structure Refinement: A Crystallographer's Guide to SHELXL*; Muller, P., Ed.; Oxford University Press: New York, 2006. (c) Sheldrick, G. M. *SHELXL-97, A program for crystal structure refinement* Göttingen, **1997**.

(11) Stoumpos, C. C.; Malliakas, C. D.; Kanatzidis, M. G. Semiconducting tin and lead iodide perovskites with organic cations: phase transitions, high mobilities, and near-infrared photoluminescent properties. *Inorg. Chem.* **2013**, *52*, 9019-9038.

(12) Angel, R. J. Equations of State. *Rev. Mineral. Geochem.* **2000**, *41*, 35-59.

(13) Giannozzi, P.; Baroni, S.; Bonini, N.; Calandra, M.; Car, R.; Cavazzoni, C.; Ceresoli, D.; L. Chiarotti, G.; Cococcioni, M.; Dabo, I.; et al. QUANTUM ESPRESSO: a modular and open-source software project for quantum simulations of materials. *J. Phys.: Condens. Matter* **2009**, *21*, 395502.

(14) Kuisma, M.; Ojanen, J.; Enkovaara, J.; Rantala, T. T. Kohn-Sham potential with discontinuity for band gap materials. *Phys. Rev. B* **2010**, *82*, 115106.

(15) Gritsenko, O.; van Leeuwen, R.; van Lenthe, E.; Baerends, E. J. Self-consistent approximation to the Kohn-Sham exchange potential. *Phys. Rev. A* **1995**, *51*, 1944-1954.

(16) Kohn, W.; Sham, L. J. Self-consistent equations including exchange and correlation effects. *Phys. Rev.* **1965**, *140*, A1133-A1138.

(17) Vanderbilt, D. Soft self-consistent pseudopotentials in a generalized eigenvalue formalism. *Phys. Rev. B* **1990**, *41*, 7892-7895.

(18) Messiah, A. *Quantum Mechanics*; North-Holland: Amsterdam, NL, 1961; Vol. II.

(19) Perdew, J. P.; Ruzsinszky, A.; Csonka, G. I.; Vydrov, O. A.; Scuseria, G. E.; Constantin, L. A.; Zhou, X.; Burke, K. Restoring the density-gradient expansion for exchange in solids and surfaces. *Phys. Rev. Lett.* **2008**, *100*, 136406.

(20) Corso, A. D.; Conte, A. M. Spin-orbit coupling with ultrasoft pseudopotentials: Application to Au and Pt. *Phys. Rev. B* **2005**, *71*, 115106.

(21) Umari, P.; Mosconi, E.; De Angelis, F. Relativistic GW calculations on $CH_3NH_3PbI_3$ and $CH_3NH_3SnI_3$ perovskites for solar cell applications. *Sci. Rep.* **2014**, *4*, 4467.

(22) Matsuishi, K.; Ishihara, T.; Onari, S.; Chang, Y. H.; Park, C. H. Optical properties and structural phase transitions of lead-halide based inorganic–organic 3D and 2D perovskite semiconductors under high pressure. *Phys. Status Solidi B* **2004**, *241*, 3328-3333.
(23) Wang, Y.; Lü, X.; Yang, W.; Wen, T.; Yang, L.; Ren, X.; Wang, L.; Lin, Z.; Zhao, Y. Pressure-induced phase transformation, reversible amorphization, and anomalous visible light response in organolead bromide perovskite. *J. Am. Chem. Soc.* **2015**, *137*, 11144-11149.